© 2020 Yangxue Yu

ROTORDYNAMIC ASSESSMENT FOR A PERMANENT MAGNET SYNCHRONOUS MOTOR

BY

YANGXUE YU

THESIS

Submitted in partial fulfillment of the requirements
for the degree of Master of Science in Electrical and Computer Engineering
in the Graduate College of the
University of Illinois at Urbana-Champaign, 2020

Urbana, Illinois

Adviser:

Associate Professor Kiruba Sivasubramaniam Haran

ABSTRACT

High speed and high rotor tip-speed, in particular, combined with high magnetic and electrical loading, are key enablers for obtaining high specific power in electric machines. The rotor described in this thesis pushes the tip speed to about 80% of the speed of sound. An outer rotor design with a carbon-fiber retaining ring on the outer diameter (OD) was chosen to maintain high magnetic loading in the airgap while ensuring structural integrity at high speed. To achieve manufactural feasibility, a cantilevered rotor structure was proposed to suspend the rotor around the stator. This architecture introduces significant rotordynamic challenges, one of which is the "trunnion effect," a rotordynamic effect uncommon in traditional electric machines. This effect was identified when a discrepancy was observed during a rotor test and a root-cause analysis was performed to explain it. The original rotor dynamic model was modified to include this effect, and verified through a ping test. The trunnion effect, which significantly reduces the critical speeds, can be offset by selecting appropriate dimensions for the rotor end plate using the revised model. Thus, even in the presence of this effect, the proposed unconventional motor topology is confirmed to function reliably.

To my parents, for their love and support.

ACKNOWLEDGMENTS

I thank Dr. Kiruba S. Haran for accepting me to his research group and for the guidance over the past two years. It is thanks to his professionalism, leadership and support that I could come to where I am.

I thank Samith Sirimanna for helping me with analyses and tests and Lijun Zheng for conducting an initial study of the trunnion effect.

I thank the Grainger Center for Electric Machinery and Electromechanics and the cooperative agreement NNX14AL79A with the NASA Glenn Research Center for the support.

I thank Collins Aerospace for providing the facility and equipment to conduct the ping test as well as for ping test data post-processing and the XLRotor model correlation review.

I thank Dr. Brian Murphy and Daniel Lubell for their technical support on XLRotor and rotordynamic analysis.

TABLE OF CONTENTS

CHAPTER 1 INTRODUCTION 1

CHAPTER 2 MOTOR DESIGN OVERVIEW 3

CHAPTER 3 ROTORDYNAMICS OVERVIEW 6
3.1 Natural Frequency 6
3.2 Resonant Frequency and Critical Speed 7
3.3 Rotordynamic Challenges of the Specific Design 8

CHAPTER 4 TRUNNION EFFECT 10
4.1 Overview 10
4.2 Trunnion Stiffness 12
4.3 2-D Model Simulation 13
4.4 Ping Test 14

CHAPTER 5 TRUNNION EFFECT AND ROTORDYNAMICS . . . 18

CHAPTER 6 FUTURE WORK 21
6.1 Analytical Model 21
6.2 Proposed Solutions 21
6.3 Future Design 22

CHAPTER 7 CONCLUSION 23

REFERENCES 24

CHAPTER 1

INTRODUCTION

Data shows that the world passenger air traffic (expressed in revenue passenger kilometres) increases at an average annual rate of 5.0 percent [1]. NASA initiated the Fixed Wing Project (aircraft) to address financial and environmental concerns caused by increasing air-traffic worldwide. A key enabling feature of both electric and hybrid-electric aircraft is electric motors with high specific power. Such motors could enable a shift from gas to electric and hybrid gas-electric propulsion, and thus the energy consumption, emissions, and noise could be significantly reduced [2]. Permanent magnet synchronous motors (PMSM) have been shown to have high efficiencies and power densities [3][4]. Thus, pushing the rotor tip speed close to the speed of sound becomes crucial for high-power PMSMs. The motor described in this thesis has pushed the rotor tip speed to 270 m/s, which is also the highest value found in the literature for PM machines [5]. This motor is a surface-mount PMSM, and it meets NASA's requirement for power, specific power, and efficiency: 1 MW, >13 kW/kg, and >96%, respectively, with the design approach and motor topology detailed in [6]. An unexpected challenge of this design is the trunnion effect observed on the rotor, which was identified from discrepancies observed in a rotor spin test.

Chapter 2 provides an overview of the motor design. Then the overall rotordynamic concerns will be described in Chapter 3. The cause of the trunnion effect will be explained in Chapter 4, where trunnion stiffness is estimated analytically. The rotor trunnion frequency is determined by a 2-D rotordynamics model. Results are verified through a ping test. The trunnion effect influence on natural frequency, and thus on critical speed, will be illustrated in Chapter 5. A modified rotordynamic model with a drivetrain was created to estimate the critical rotor speed, which is found to be notably lower than that predicted by the original model (without trunnion effect). Two approaches will be introduced to offset (increase or reduce) the

critical speed to a proper range.

This work has been submitted to the International Conference on Electrical Machines (ICEM), 2020 [7], and is adapted here with permission.

CHAPTER 2

MOTOR DESIGN OVERVIEW

A motor topology has been chosen to meet NASA's lightweight, high-specific-power, high-power, and high-efficiency specifications. A self-pumped air-cooling design was selected to meet the weight requirement. Heat generated by bearing friction, and by windage and electrical losses, is removed by the air flowing through the heat sink and airgap, thus eliminating the need for an extra cooling system. The air flow is generated by the pressure drop resulting from a centrifugal fan [8]. Iron usage was reduced dramatically by three design choices to meet the lightweight and high-specific-power objectives. *Specific power refers to the ratio between motor output power and weight.* A high-pole-count motor topology was chosen because it reduces the thickness of both stator and rotor yoke. The rotor yoke could then be eliminated by a Halbach magnet array, a magnet arrangement that forms self-contained flux paths. An outer rotor design, with the rotor being outside the stator and thus getting rid of the retaining ring between the rotor and stator, was adopted to satisfy the high-power and high-speed operation. This increases motor performance by reducing the airgap. Extra iron losses are generated due to high frequency, a combined result of high pole count and high operating speed. Slotless windings were used to reduce this loss, and in turn shrank the stator yoke volume. Structural stability and ease of manufacturing were accomplished by a cantilevered rotor shell design. Table 2.1 lists the key motor features.

Figure 2.1 shows an axial-cross section of the 3-D motor model, with all the key components labeled, and Figure 2.2 shows key rotor shell features. Blue shades indicate the rotating parts and orange the stationary parts. A thin titanium rotor shell holds the neodymium magnet arrays in place. Catastrophic failure caused by excess stress, a result of centrifugal force under high-speed operation, is avoided with the addition of a high-strength carbon fiber retaining ring. The hub serves as the connection to the drivetrain. Two

Table 2.1: Motor key features

Parameter	Symbol	Value	Unit
Rated power	P_{rate}	1	MW
Rated efficiency	η_{rate}	96.4%	
Specific power	1111	15	kW/kg
Nominal speed	ω_m	15000	rpm
Pole pair	p	10	
Retaining ring thickness	t_{cf}	0.0129	m
Rotor outer radius	R_o	0.1591	m
Magnet outer radius	R_m	0.1552	m
Rotor inner radius	R_i	0.1423	m

angular-contact ball bearings located at both ends of the inner shaft connect the rotor to the stator. Air enters from the free area at the winding leads, goes through the airgap and heat sink, and exits from the rotor shell at the fan holes. The air-flow path is shown in red in Figure 2.1.

Models of expansion, windage loss, and rotordynamics were created to understand the motor performance and validate the design concepts. Tests were performed to confirm the model accuracy [9]. During the rotordynamic test, the prototype rotor was balanced and spun up to 18000 rpm with no ill effects. A discrepancy between the rotordynamic model and test results was observed. With further study, it is suggested that the discrepancy might be attributed to a trunnion effect at the rotor [10].

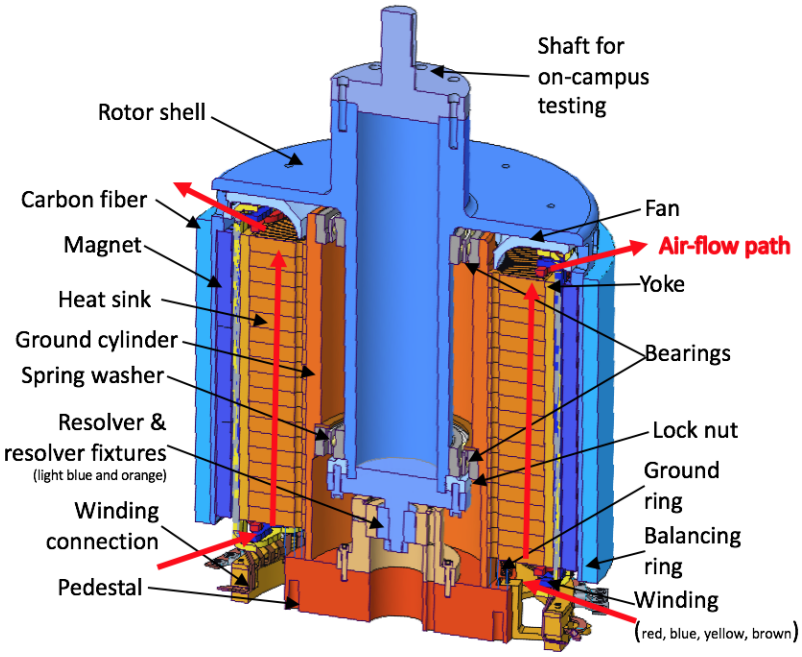


Figure 2.1: Motor model with components labeled

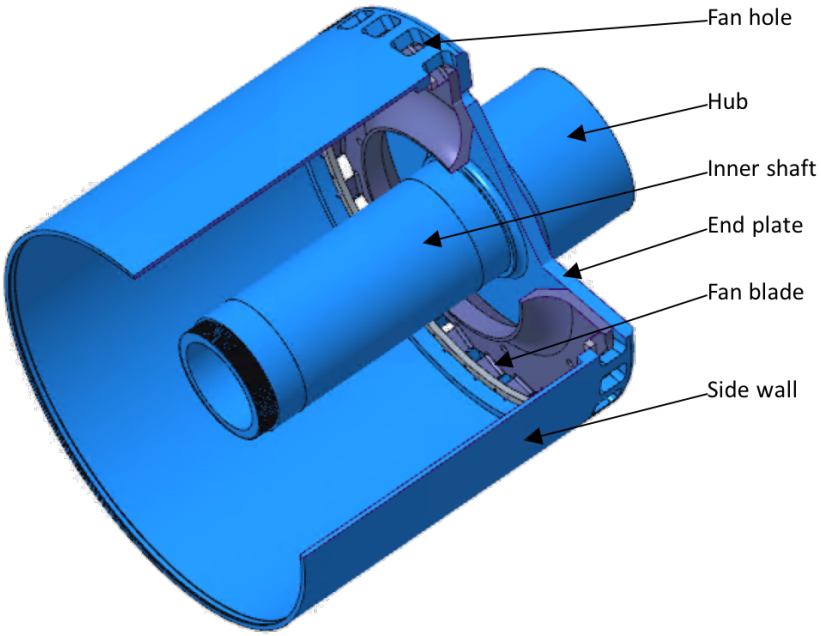


Figure 2.2: Rotor and fan with features labeled

CHAPTER 3

ROTORDYNAMICS OVERVIEW

The study of rotordynamics for high-speed machines is particularly important because any undesired dynamic behavior of the system, including the motor and the drivetrain, may create catastrophic failure. A good understanding of rotordymanics helps to predict the critical speed, at which the system is excited and may experience large vibration. If the predicted value does not fall within the acceptable critical speed range, the machine could be modified or optimized during the design phase; this avoids devoting excessive time and money to make a change during/after manufacturing.

3.1 Natural Frequency

Before diving into critical speed and resonant frequency, the concept of natural frequency should be introduced. *It refers to the frequency at which the object tends to vibrate under an external force, like being hit, struck, strummed, etc.* It could be one frequency or a set of frequencies depending on the degree of freedom of the object. It is a characteristic of the object, and the natural frequency magnitude(s) are completely results of the mass and stiffness value and distribution.

There is always a set of natural frequencies for an object with complex geometry and connections, for example, the rotor described in the thesis. Two categories of modes can be defined among the natural frequencies: rigid-body mode and flexible mode. Zero hertz corresponds to the natural frequency for a rigid-body mode, a mode in which no deformation is observed. Of interest to us are the flexible modes of an object, where the corresponding natural frequencies are not zero. Under flexible modes, the object undergoes deformation, i.e., it vibrates. These natural frequencies can be numerically analyzed through XLRotor, a 2-D rotordymanic modeling software, and physically

tested by ping test.

Ping test is widely used to assess the natural frequency (or frequencies) of an object or a system. The main idea is to create a free condition of the object or system, which means *the object is floating in space with no attachment to ground and exhibits rigid body behavior at zero frequency, i.e. no external boundary conditions [11].* However, this is infeasible in a real-world situation. One way to approximate this free condition is to suspend the object/system in the air from very soft elastic cords or place it on a very soft cushion. Due to the nonideal free condition during the test, some rigid-body modes might have a nonzero frequency. If the highest rigid-body mode frequency is less than one tenth of the first flexible mode frequency, the test result is credible.

3.2 Resonant Frequency and Critical Speed

For rotating machines, there are two frequencies: forward and backward, at each mode shape. The two have the same value at zero shaft speed (natural frequency). When the shaft speed increases, the two split into two directions, which results in forward whirling mode and backward whirling mode, respectively. This is due to the gyroscopic effect, which is the tendency of a rotating object to maintain a steady direction of its axis of rotation. For forward whirling mode, energy is extracted from the system, which causes a reduction in kinetic energy, and the gyroscopic effect tends to raise the corresponding forward whirling frequency [12][13]. For backward whirling mode, energy is added to the system, thus decreasing the corresponding backward whirling frequency. In reality, the backward whirling mode is not excited and does not contribute to large vibration; therefore, it is not of interest [14].

Resonant frequency refers to the frequency at which the forced frequency meets the natural frequency, and thus the object/system's vibration magnitude increases manifold. In the case of a rotational system, the resonant frequency is captured at the intersection between the system's synchronous frequency and its natural frequencies (forward and backward). However, as mentioned above, only forward ones are considered here. Critical speed is the resonant frequency expressed in *revolutions per minute (rpm).* For this design, only the first critical speed is concerned. More will be explained in

Section 3.3.

Generally, the resonant frequency can be characterized by the following: P, the ratio of the polar moment of inertia I_p to the transverse moment of inertia I_t; ω, the synchronous rotational speed; L, the distance between bearings; and I_t, defined previously [9].

$$\omega_n = -\frac{I_p \omega}{2} \pm \sqrt{(\frac{P\omega}{2})^2 + \frac{kL^2}{2I_t}} \tag{3.1}$$

Acknowledging the complexity of the rotor and the drivetrain, this equation is only used during the initial design phase. Later on, numerical analysis of resonant frequency using XLRotor was performed.

3.3 Rotordynamic Challenges of the Specific Design

The rotor brings rotordynamic challenges. Unlike the conventional inner rotor configuration, which has the rotor symmetrically supported by two bearings on both sides of the rotor, this rotor is cantilevered at two bearings with a thin radial build (a heavy array of neodymium magnets on the inner rotor shell and a carbon fiber sleeve on the outer rotor shell) and operates at 15,000 rpm. Figure 3.1 shows a rotor model in XLRotor with the bearing positions marked. The critical speed, determined by the entire drivetrain—motor, coupling, and drive shaft—is always smaller than the rotor natural frequency, because with the addition of components and connections, the system stiffness is reduced. The machine can run beyond the harmonics with no ill effect if it is well balanced. However, this practice is not preferred. Two approaches to avoid rotordynamics failure without relying exclusively on balancing are: (1) designing for a high critical speed such that at least 25% margin is saved between the critical and operating speed [15], and (2) designing for a low critical speed which can pass through the system vibration limit to reach the operating speed. Approach (1) was selected for rotordynamic design of this project.

For test validation of the rotordynamic analysis, it is unrealistic to perform a pin test with the overall drive system. Knowing that the rotor has the most uncertain dynamic behavior and is the key contributor to the system critical speed, our team decided to build two rotordynamic models: one

including rotor only with free condition, and one including all the components in the system with bearings and supports. The accuracy of the numerical model is verified through comparison between the former model and the ping test results of the rotor. Once the rotor-only model is verified, the rotor characteristics are carried to the second model and the system dynamic behavior can be studied.

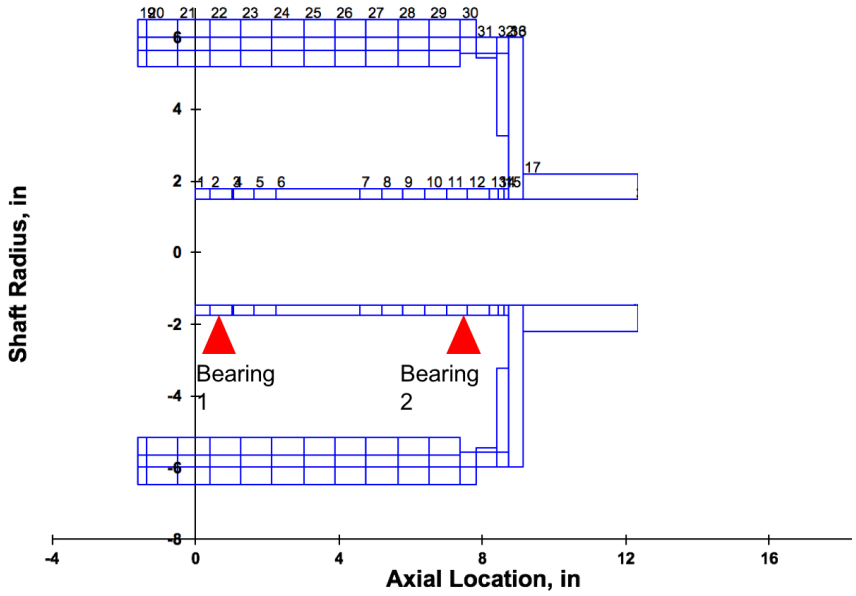


Figure 3.1: Rotor 2-D model with bearing locations marked

CHAPTER 4

TRUNNION EFFECT

4.1 Overview

The trunnion effect exists at stepped shaft sections with thin side walls [16]. The plate, where the trunnion sits, deforms as a disk supported at the edges when a bending moment is applied to the trunnion, as shown in Figure 4.1. Because this effect significantly reduces the angular stiffness of the section, it has become an important consideration when designing rotating machinery.

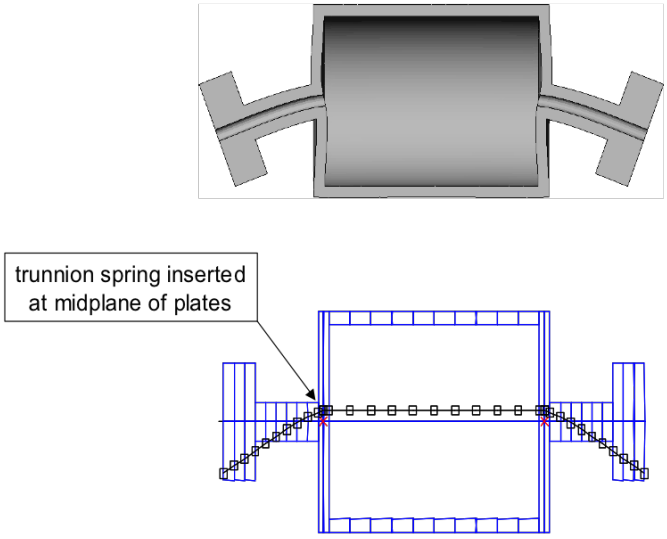


Figure 4.1: Trunnion effect illustration and XLRotor example [17]

In general, it can be treated as a flexible-disk-coupling problem and is modeled as circular plates with different conditions. Various models developed in the literature are summarized in [18]. Among these models, [19] shows that the object (plate and trunnion) excitation frequency is increased when the plate is thickened.

Several studies on turbine shaft failure reveal the importance of proper

rotordynamic analysis at the trunnion section, though not many cases can be reported and analyzed in the literature due to confidentiality [20]. In [21], failure analysis on a 28 MW bulb turbine shows the crack section as shown in Figure 4.2. The long shaft could be considered as a trunnion and the open end is the plate; the crack is at the section where the trunnion joins the plate. Another failure analysis was performed on the scroll conveyor trunnion shaft of a solid bowl centrifuge; a crack, shown in Figure 4.3, was identified at the trunnion joint [22]. Other than improving the operating condition and manufacturing procedure, both articles suggest that the shaft should be redesigned to reduce the stress concentration at the crack zone. This implies increasing angular stiffness at the outer peripheral portion of the plate, as [23] shows that stress decreases with the increase of the stiffness.

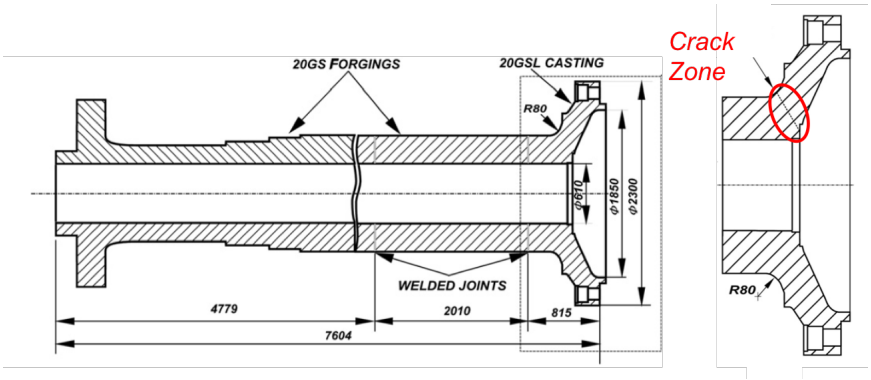


Figure 4.2: Longitudinal cross section of the shaft [21]

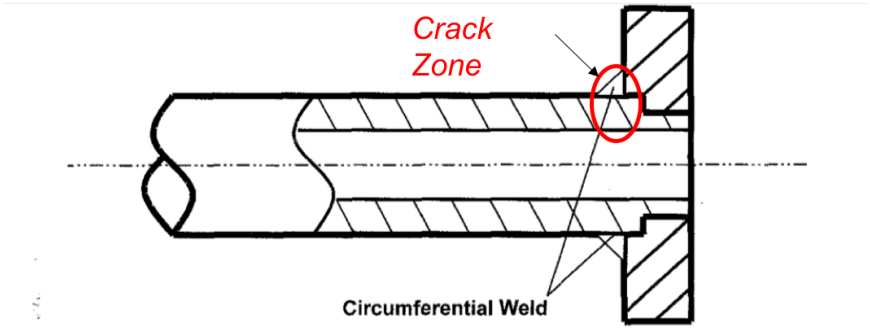


Figure 4.3: Longitudinal cross section of the shaft [22]

In the case of this motor, both the hub and the inner shaft are considered as trunnions and thus can cause deformation of the rotor end plate. The rotational stiffness due to the trunnion was determined analytically to

characterize the trunnion effect. A free-condition rotordynamic model was created to characterize the rotor trunnion frequency using XLRotor. The results were verified by a ping test.

4.2 Trunnion Stiffness

The model and the equations to estimate the trunnion stiffness in [17] were used. Equation parameters, including the plate thickness t, the wall thickness h, the shell inner radius a, and the hub radius b, were adjusted to represent our rotor geometry. In the context of the physical meaning of the trunnion effect, the inner rotor shell radius and the rotor shell thickness were substituted into the equation parameters, a and h, respectively. The overall rotor thickness (magnet, rotor shell, and retaining ring) was not used because it did not contribute to the edge support. The supporting edge is at the corner where the titanium shell meets the titanium end plate, and only the rotor shell presents at the corner, which contributes to the stiffness. Pinned support at the edge was assumed to be conservative with the analytical estimation. Table 4.1 shows the parameters and values that were substituted in Equation (4.1) and (4.2).

Table 4.1: Parameters used for trunnion stiffness estimation

Parameter	Symbol	Value [m]
Hub outer radius	b	0.0555
Rotor shell inner radius	a	0.1422
Rotor end plate thickness	t	0.0178
Rotor shell thickness	h	9.77xE-3

$$K_{pinned} = \frac{\pi E t^3}{3(1-\mu^2)}\left(\frac{2(\beta^2-1)+\mu(\beta^2-1)^2}{(3+\mu)+(1-\mu)\beta^4} - ln(\beta)\right)^{-1} \tag{4.1}$$

$$\beta = \frac{b-0.5t}{a+0.5h} \tag{4.2}$$

where E is the elastic modulus, and μ is Poisson's ratio. Because the components affecting the trunnion stiffness (the rotor shell and the fan) are made of Ti_6Al_4V titanium, material properties of titanium were used. The estimated trunnion stiffness is $1.09 * 10^6$ Nm/rad.

4.3 2-D Model Simulation

A 2-D model was built in XLRotor for analyzing the free-condition mode frequencies. In this case, analysis is done only at zero speed and only the rotor structure is modelled. The prototype rotor requires an eyebolt to connect hang the rotor in air. This was included in the model with a rigid connection. The 2-D model is shown in Figure 4.4. The first flexible frequency was found to be 598 Hz (Table 4.2), and the result is illustrated in Figure 4.5, which corresponds to trunnion effect. It should be noted that the third mode listed in the table, though having a nonzero mode frequency, is a rigid-body mode. The nonzero frequency is likely the result of the non-absolute free condition in the analysis constraints.

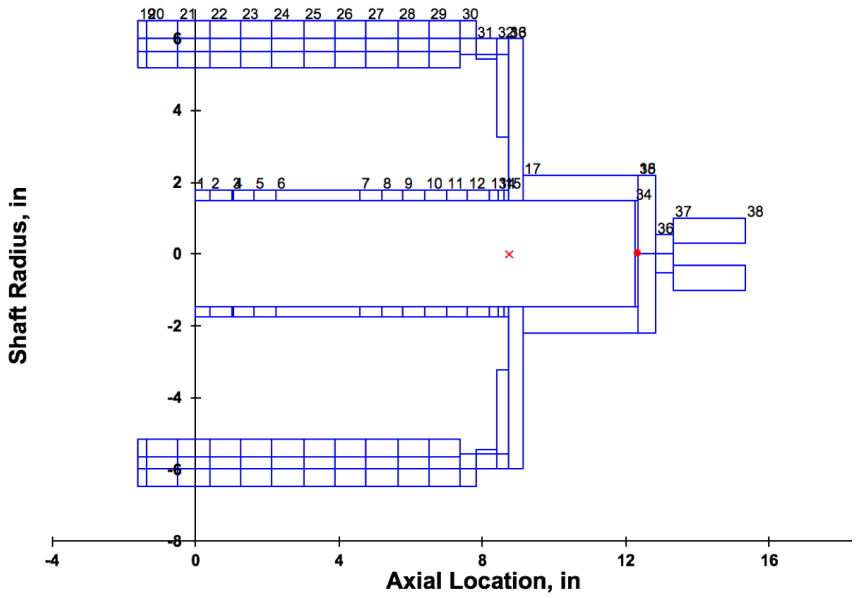


Figure 4.4: XLRotor model setup

Table 4.2: Natural frequencies from XLRotor

Mode	rpm	Hz
1	0.0	0.0
2	0.0	0.0
3	4.6	0.1
4	35882	598
5	115157	1919

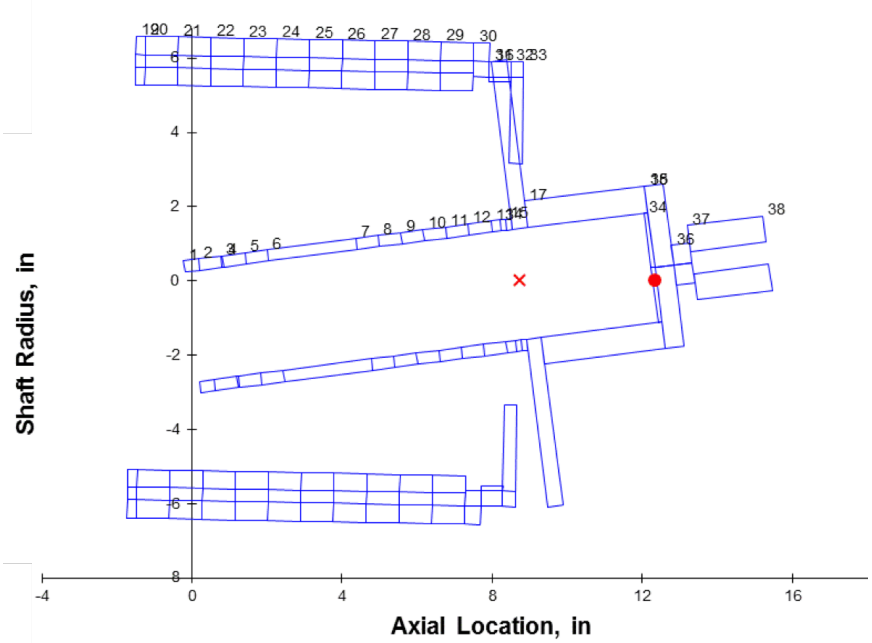


Figure 4.5: Mode shape at 598 Hz

4.4 Ping Test

Once the model is built in XLRotor, an easy way to validate the model is by performing a ping test. If the expected free-free mode frequencies from the model and the results from the ping test match well, that confirms the accuracy of the model.

The test setup is shown in Figure 4.6. The rotor hub was attached to an eyebolt connection feature, which was hung through a steel chain to approximate the free-free condition. Accelerometers were attached to the rotor surface using petro wax. An impact hammer was used to excite the rotor. An analyzer, Data Physics SignalCalc 730, was used to collect the data from the accelerometers and the impact hammer. Averaged frequency response was automatically generated by the analyzer. Rotor displacements at the outer surface were measured approximately every 2.5 cm starting from the open end, and at the end of the inner shaft (Figure 4.7). For each axial position measurement, an average of five hits was taken. Each hit was carefully made such that the hitting strength was even and the hitting direction was perpendicular to the rotor shell. The excitation point was right above the accelerometer at the end of the rotor shell (red dot in Figure 4.7).

Figure 4.8 shows the frequency response of the ping test. The mode shapes

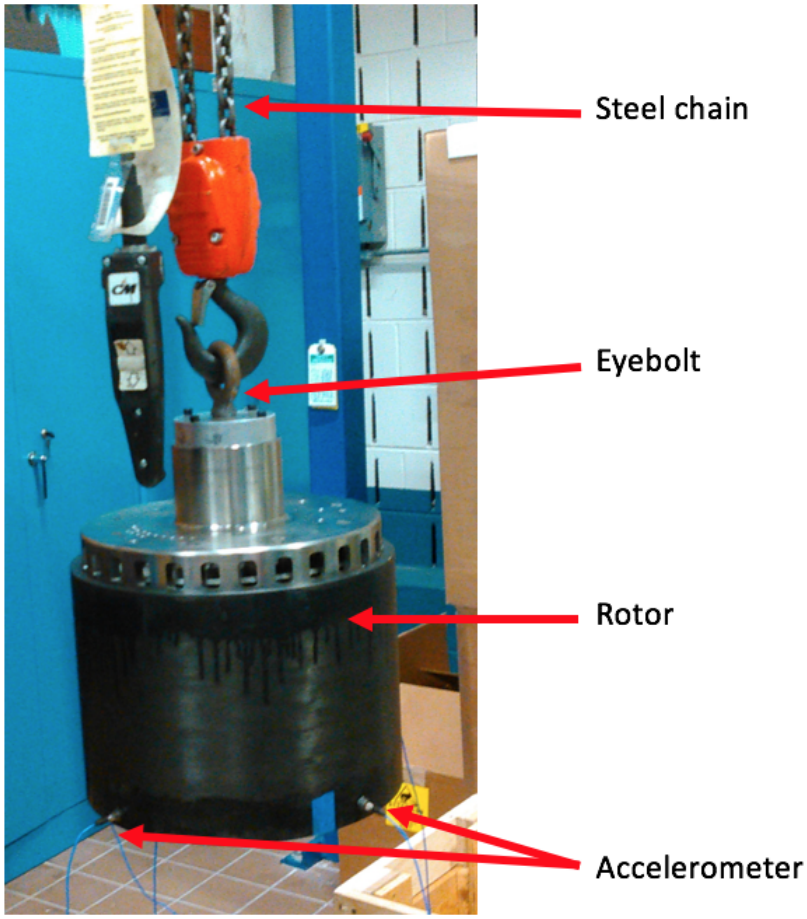


Figure 4.6: Test setup

at frequencies where FFT has a peak were plotted to examine the trunnion effect, using ME'scope. At frequency 590 Hz, a see-saw mode shape was observed at the inner shaft and the hub (Figure 4.9). This corresponds to a trunnion mode shape and verifies that 590 Hz is the free-free rotor (with eye-bolt) trunnion frequency. The two results, rotordynamic model and the test, show extreme agreement and provide solid evidence of the trunnion effect existence.

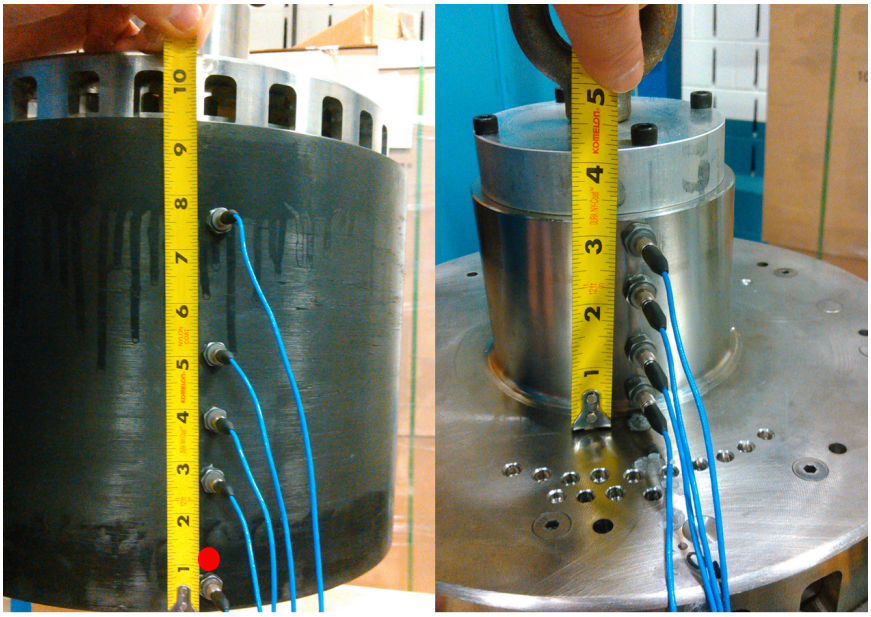


Figure 4.7: Example of accelerometer positions for ping test

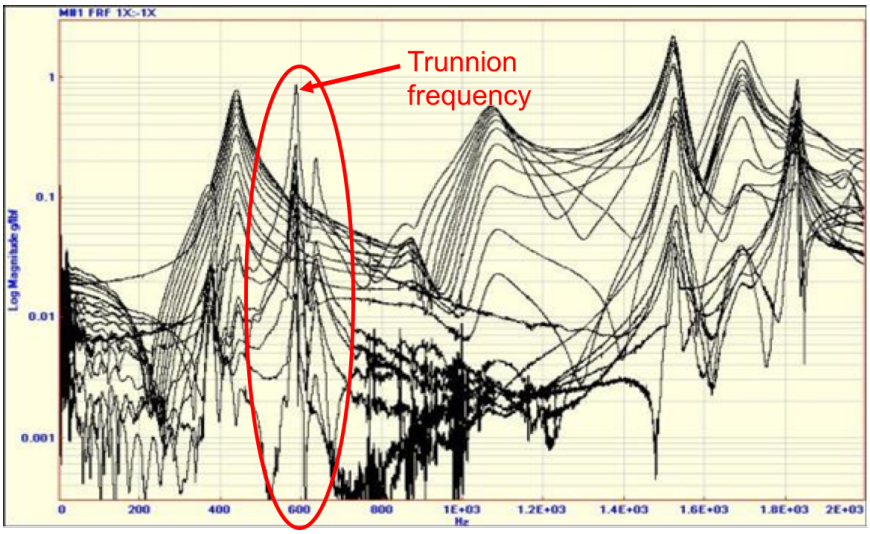


Figure 4.8: FFT plot of ping test

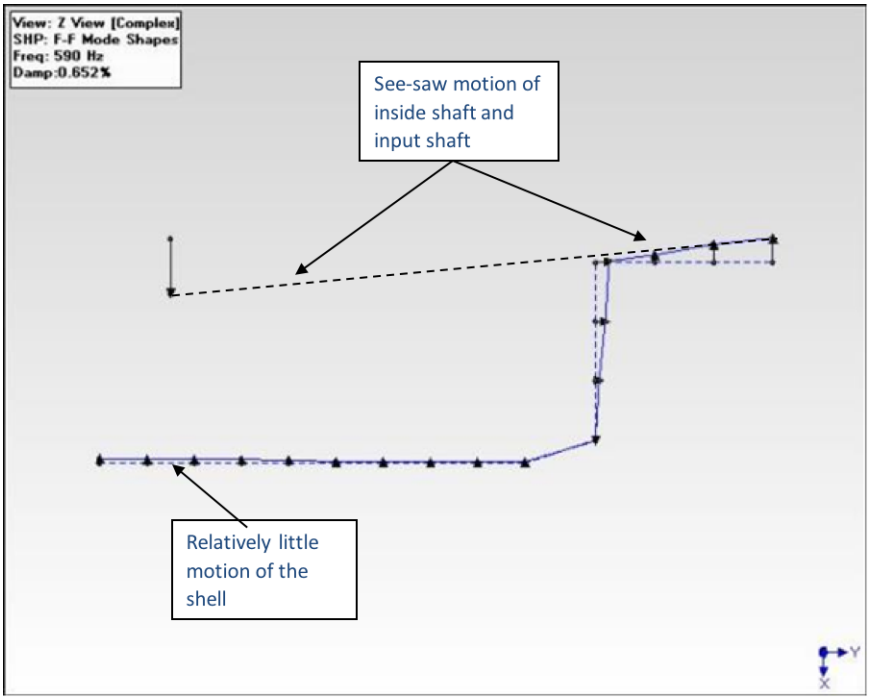


Figure 4.9: Free-free trunnion mode shape, observed at frequency 590 Hz

CHAPTER 5

TRUNNION EFFECT AND ROTORDYNAMICS

The trunnion effect further reduces the system stiffness, and thus the critical speed. This causes the risk of insufficient or negative margin between the critical and operating speed.

Figure 5.1 shows the drive-train model in XLRotor. Small vertical sections (beams) were used to represent various aspects of the rotor and drive-train structure. Stiffness values for bearings were provided by the manufacturing datasheet and trunnion stiffness was kept as a control variable. The red x's show the bearing connections. Lines connecting the x-axis and rotor structure represent a rigid connection to ground or to a stable permanent structure.

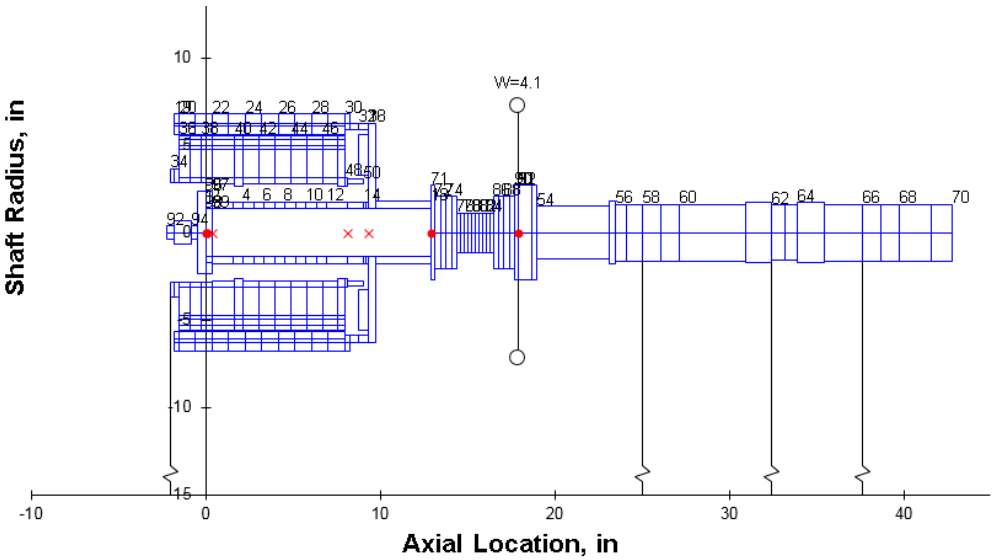


Figure 5.1: Driveline analysis setup for XLRotor

Simulations were performed for two cases, with and without the trunnion effect. Figure 5.2 shows the damped frequency plot for the motor and drivetrain. As expected, the excitation frequency for the rotating structure increases with speed due to gyroscopic effects. Two lines corresponding to

the first bending mode show the two cases of forward and backward whirl. At zero speed, these converge to the same frequency. As the speed increases, the forward whirl excitation curve moves with a larger gradient compared to the backward whirl. In the test setup, the backward whirl is experienced only when decelerating or stopping the motor; emphasis is given to the point where the forward whirl of the first mode crosses the synchronous frequency. Crossing points for other bending modes were observed to be far from the operating speed. Thus, they were not investigated as a potential scenario.

Figure 5.3 shows the damped frequency plot without trunnion stiffness. Similarly, only the intersection of the first forward mode and the synchronous frequency was of interest. The critical speeds are found to be 11,000 rpm with trunnion effect and 18,000 rpm without. Thus not characterizing the trunnion effect at the design phase results in unsafe operation at the rated speed. This shows the trunnion effect is significant and must be included in the rotordynamic analysis.

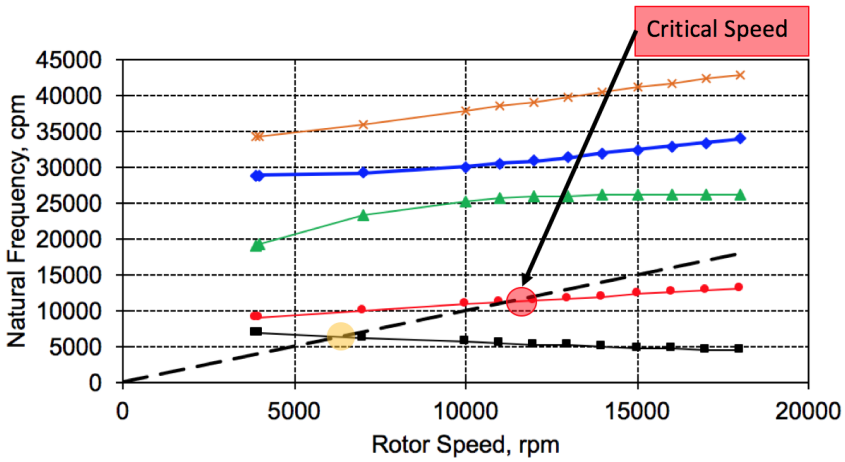


Figure 5.2: Driveline frequency model with trunnion effect

Two solutions were proposed. The rotor could be stiffened to bring up the critical speed by adding features at the rotor end plate. This essentially increases the end-plate thickness, and thus the trunnion stiffness. XLRotor shows that the critical speed could be pushed to 18,000 rpm if the end plate were three times the current thickness. Or, the rotor assembly could be modified such that the rotor stiffness is reduced. This decreases the critical speed to a point that the motor can safely pass through. The second method involves radical changes to the rotor design, including bearings and support-

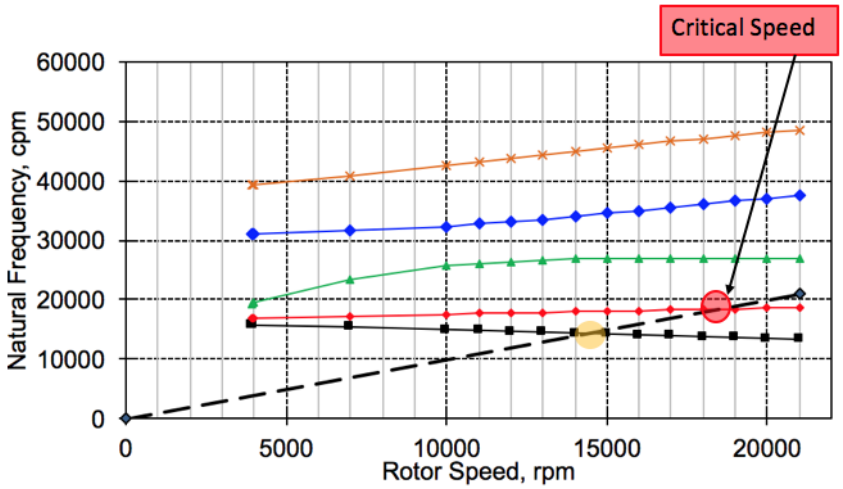


Figure 5.3: Driveline frequency model without trunnion effect

ing structures. However, it can be seen that the concept of an inside-out, cantilevered rotor configuration is valid even in the presence of the trunnion effect.

CHAPTER 6

FUTURE WORK

Though the trunnion effect has been successfully captured from both analytical calculation and physical testing, there is more to discover and verify.

6.1 Analytical Model

The analytical model used in this thesis was adapted from a typical rotor model, which does not have the exact geometry as the rotor described in Chapter 2. Several equation parameters were adjusted based on the understanding of trunnion effect and trunnion stiffness to represent this specific rotor. Yet, a more accurate model that fits the geometry of this kind of rotor (inside-out, cantilevered) should be built. This will benefit future designs, which require an inside-out, cantilevered rotor geometry to achieve high specific power.

6.2 Proposed Solutions

The two ways to relieve the high critical speed mentioned in the previous chapter both create new problems. Adding the end-plate thickness to three times the original value is essentially increasing the machine weight, which leads to reduced specific power. Further analysis could be performed on adding angle brackets between the end plate and the hub, which equivalently increases the end plate thickness without adding excessive weight. The second method requires decreasing the end plate thickness, which involves structural concerns. Ways to reduce the trunnion stiffness without affecting structural integrity should be explored.

6.3 Future Design

Selecting a bearing with very high stiffness and carefully designing the motor weight distribution could also help to avoid the presence of large critical speed within the operating range. Since the rotor described here has been manufactured and bearing related structures were already defined, neither changing the bearing nor modifying weight distribution is a feasible path. However, in future designs, the trunnion effect could be incorporated into the initial design phase. These two paths could then be considered as possible ways to effectively minimize the negative rotordynamic influence caused by trunnion effect.

CHAPTER 7

CONCLUSION

When a rotordynamic assessment for the inside-out, high-speed PMSM was made and the spin test data was analyzed, discrepancies were found between the physical and predicted results. Previous work suggests that the discrepancy can be attributed to the trunnion effect on the rotor, due to its cantilevered external rotor structure [10]. An analytical model was constructed to include this effect, which was verified by a physical ping test. It was discovered that the negative influence on system critical speed (motor and drive) can be solved by increasing the end-plate thickness or modifying the initial assembly design. Thus the rotor can still maintain its structural integrity while operating at high speeds. In future designs involving cantilevered external rotors, the trunnion effect should be taken into consideration during the initial design phase and thus assure that the required critical speed is obtained. The work reported in this thesis validates the motor topology of an unconventional cantilevered external rotor, specially designed to have high electromagnetic performance and reach a high rotor tip speed. High tip speed enables high specific power and efficiency goals to be achieved, thus ensuring that the requirements for electrified aviation are met.

REFERENCES

[1] *World Aviation and the World Economy*, Std., (accessed February 18, 2020), https://www.icao.int/sustainability/Pages/Facts-Figures WorldEconomyData.aspx.

[2] R. Rosario, "A future with hybrid electric propulsion systems: A NASA perspective," *Turbine Engine Technol. Symp. Strategic Vis. Workshop*, pp. 1–21, 2014.

[3] J. Shen, X. Qin, and Y. Wang, "High-speed permanent magnet electrical machines—applications, key issues and challenges," *CES Transactions on Electrical Machines and Systems*, vol. 2, no. 1, pp. 23–33, 2018.

[4] Q. Li, T. Fan, Y. Li, Z. Wang, X. Wen, and J. Guo, "Optimization of external rotor surface permanent magnet machines based on efficiency map over a target driving cycle," in *2017 20th International Conference on Electrical Machines and Systems (ICEMS)*. IEEE, 2017, pp. 1–5.

[5] A. Borisavljevic, *Limits, Modeling and Design of High-speed Permanent Magnet Machines*. Springer Science & Business Media, 2012.

[6] A. Yoon, X. Yi, J. Martin, Y. Chen, and K. Haran, "A high-speed, high-frequency, air-core PM machine for aircraft application," in *2016 IEEE Power and Energy Conference at Illinois (PECI)*. IEEE, 2016, pp. 1–4.

[7] Y. Yu, S. Sirimanna, K. Haran, T. Clydesdale, B. Sharos, D. Lubell, and B. Murphy, "Rotordynamic assessment for an inside out, high speed permanent magnet synchronous motor," in *2020 International Conference on Electrical Machines*. IEEE, 2020.

[8] X. Yi, R. Sanchez, K. Haran, J. Veres, A. T. Perry, and P. J. Ansell, "Self-pumped air-cooling design for a high-speed high-specific-power motor," in *2018 IEEE Transportation Electrification Conference and Expo (ITEC)*. IEEE, 2018, pp. 274–279.

[9] R. Sanchez, A. Yoon, X. Yi, L. Zheng, Y. Chen, K. S. Haran, A. Provenza, and J. Veres, "Mechanical validation of a high power density external cantilevered rotor," *IEEE Transactions on Industry Applications*, vol. 54, no. 4, pp. 3208–3216, 2018.

[10] L. Zheng, "Mechanical design and validation of 1 MW permanent magnet synchronous machine," Ph.D. dissertation, University of Illinois at Urbana-Champaign, 2018.

[11] Agilent Technologies, "The fundamentals of modal testing," technical report, 2000.

[12] *Whirl Speed and Stability Results*, (accessed February 18, 2020), https://dyrobes.com/help1800/Rotor/html/dyro4a0d.htm.

[13] T. Náhlík and D. Smetanová, "Applications of gyroscopic effect in transportation," *NAŠE MORE: znanstveno-stručni časopis za more i pomorstvo*, vol. 65, no. 4, pp. 293–296, 2018.

[14] Y. Chen and J. Jiang, "Effects of forward/backward whirl mechanism on nonlinear normal modes of a rotor/stator rubbing system," *Journal of Vibration and Acoustics*, vol. 137, no. 5, 2015.

[15] W. Tong, *Mechanical Design of Electric Motors*. CRC press, 2014.

[16] M. Darlow, B. Murphy, J. Elder, and G. Sandor, "Extension of the transfer matrix method for rotordynamic analysis to include a direct representation of conical sections and trunnions," *Journal of Mechanical Design*, vol. 102, no. 1, pp. 122–129, Jan 1980.

[17] J. M. Vance, F. Y. Zeidan, and B. G. Murphy, *Machinery Vibration and Rotordynamics*. John Wiley & Sons, 2010.

[18] S. Feng, B. Yang, Y. Qi, H. Geng, and L. Yu, "Angular stiffness of a trunnion joint," in *2019 IEEE International Conference on Mechatronics and Automation (ICMA)*. IEEE, 2019, pp. 314–318.

[19] L. Pope, "Response of a mindlin plate with trunnion," *Journal of Sound and Vibration*, vol. 71, no. 1, pp. 17–31, 1980.

[20] N. Bachschmid, P. Pennacchi, and E. Tanzi, *Cracked Rotors: A Survey on Static and Dynamic Behaviour Including Modelling and Diagnosis*. Springer Science & Business Media, 2010.

[21] D. Momčilović, Z. Odanović, R. Mitrović, I. Atanasovska, and T. Vuherer, "Failure analysis of hydraulic turbine shaft," *Engineering Failure Analysis*, vol. 20, pp. 54–66, 2012.

[22] T. Nguyen, M. Romios, and O. Es-Said, "Failure of a conveyor trunnion shaft on a centrifuge," *Engineering Failure Analysis*, vol. 11, no. 3, pp. 401–412, 2004.

[23] B. Zhang, Y. Zhan, S. Feng, H. Geng, J. Zhou, L. Yu, and W. Cheng, "Stress of a trunnion joint," in *2016 IEEE International Conference on Mechatronics and Automation*, 2016, pp. 1771–1775.